AIAA AVIATION Forum
June 27-July 1, 2022, Chicago, IL & Virtual
AIAA AVIATION 2022 Forum

10.2514/6.2022-3253

The Spectral Decomposition of Skewness in the Turbulent Boundary Layer

S. Midya, F. O. Thomas, M. Lozier and Gordeyev S.

Institute for Flow Physics and Control, University of Notre Dame, Notre Dame, IN, USA

In this paper the skewness of streamwise velocity fluctuations in a canonical zero pressure gradient turbulent boundary layer is spectrally decomposed via the bispectrum. In particular, it is shown that the real part of the bispectrum allows the individual triad interactions contributing to the skewness to be characterized. These measurements are presented for a range of wall-normal locations associated with positive, zero and negative skewness. The individual contributions are also summed to obtain partial and cumulative sums of the skewness as a function of frequency. Complementary conditional sampling measurements demonstrate that the main contribution to boundary layer skewness is intimately associated with ejection-sweep and sweep-ejection events and the degree of asymmetry of their characteristic velocity signatures.

Nomenclature

B_{xxx}	=	bispectrum
C_f	=	skin friction coefficient
f	=	frequency
f^*	=	characteristic large eddy frequency ($f\ \delta/U_\infty$)
f^*_{+Ve}	=	most probable frequency of positive skewness producing VITA events
f^*_{-Ve}	=	most probable frequency of negative skewness producing VITA events
H	=	boundary layer shape factor
Re_θ	=	$U_\infty\ \theta/\upsilon$
Re_τ	=	$u_\tau\ \delta/\upsilon$
U_∞	=	freestream velocity
u	=	streamwise velocity fluctuation
u_τ	=	friction velocity
$x(t)$	=	time-series data
$\widehat{x_{f^*}}$	=	temporal Fourier transform of x(t)
δ	=	boundary layer thickness
θ	=	boundary layer momentum thickness
$\overline{(\ )}$	=	time average quantity

I. Introduction

There has now developed a general consensus that large-scale structures in wall bounded turbulent flows play a key role in governing the flow dynamics and their importance in technologically relevant flow properties (e.g friction drag, noise generation, aero-optical distortions, flow separation etc.) is widely acknowledged. The nature of the large-scale motions was the topic of the review by Robinson [1]. The interaction between outer large-scale motions and near-wall turbulence is widely recognized. Hutchins and Marusic [2,3] demonstrated that near wall turbulence is modulated by the outer large-scale motions. This amplitude modulation of near wall turbulence was characterized by Mathis et al

[4]. Their study correlated a low-pass filtered outer region signal with the envelope function of the near-wall, small-scale velocity fluctuations obtained via a Hilbert transform. The resulting profile of the normalized amplitude modulation correlation coefficient was found to bear a very strong resemblance to the corresponding velocity skewness profile. This similarity between the skewness and amplitude modulation correlation coefficient was further explored by Mathis et al [5]. Using a scale decomposed signal given by $u^+ = u_L^+ + u_S^+$ where superscript + denote inner variable scaling, subscripts *L* and *S* denote large- and small-scale contributions, respectively, they showed that a significant contribution to the skewness is the cross term $3\,\overline{u_L^+ u_S^{+\,2}}$ where an overbar indicates a time-mean quantity and $\tilde{X} \equiv \bar{X}/\left(\overline{u^{+2}}\right)^{3/2}$. They suggest the cross-term can be used as an alternative diagnostic tool for the characterizing the amplitude modulation of near-wall turbulence by the large-scales.

It is clear that skewness of the streamwise velocity signal is an important parameter in turbulent boundary layers. It is intrinsically related to the quadratic energy transfer mechanism since only triadically coupled modes make non-zero contributions to the skewness. Skewness is also intimately related to the interactions between different spatial scales present in the turbulent boundary layer flow as described above. Given this importance, this paper examines the spectral decomposition of the skewness in a zero-pressure gradient turbulent boundary layer. This decomposition is achieved via the real part of the bispectrum and provides a measure of the modal contribution to the skewness at different characteristic wall-normal locations. The relation between the skewness and the bispectrum is described below.

II. Skewness and the Bispectrum

Like the spectral decomposition of the second moment via the autospectral density function, one can decompose the skewness in frequency domain using the third-order spectral estimate known as the bispectrum. The bispectrum captures the triadic interactions between the frequencies present in the flow. The bispectrum is defined as,

$$B_{xxx}(f_1^*, f_2^*) = E\left[\hat{x}_{f^*}^C, \hat{x}_{f_1^*}, \hat{x}_{f_2^*}\right] \tag{1}$$

where,

$$f^* = f_1^* + f_2^* \tag{2}$$

Here $E[\ ]$ denotes an expected value, $\hat{x}_{f_1^*}$ a temporal Fourier transform of time series *x*(t) and the superscript C denotes a complex conjugate. In the application of the bispectrum to be used in the boundary layer here, the frequencies have been normalized by the characteristic large-eddy frequency ($f_i^* \equiv f_i\,\delta\,/U_\infty$). Owing to its symmetry properties (e.g Rosenblatt and Ness [6], Kim and Powers [7], Elgar [8]) it is sufficient to compute the bispectrum for the triangular frequency domain shown in Figure 1. This triangular region is associated with triad sum interactions. For example, point A is associated with the sum interaction between two different frequencies f_h^* and f_k^* which gives rise to $f_{sum}^* = f_h^* + f_k^*$. However, the corresponding two difference interactions involving the same wave triad would also map to the same point. It is shown by Elgar [8] that the real part of the bispectrum is related to the third moment by,

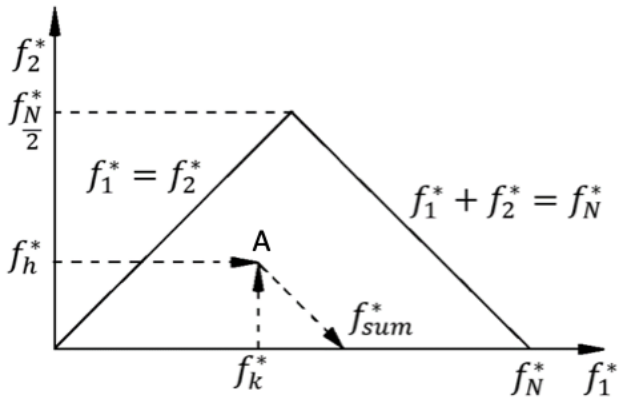

Figure 1. Region of computation of the auto-bispectrum. Only the sum interaction region is shown.

$$E(u^3(t)) = \sum_{f_1^*} \sum_{f_2^*} Re\left(B_{xxx}(f_1^*, f_2^*)\right) \qquad (3)$$

where the sum is taken over the whole range of f_1^* and f_2^*. The real part of the bispectrum provides the contribution to the third moment from the wave triad (f_1^* , f_2^* , $f_1^* + f_2^*$). Hence, the decomposition of the third moment in frequency domain via equation (3) reveals information regarding the specific wave triads undergoing nonlinear interaction, thereby providing a new perspective on the nature of the contribution of different modes to the skewness. In fact, for the triangular region shown in Figure 1, the third moment is given by the following equation (Rosenblatt and Ness [9], Elgar and Guza [10]),

$$E(u^3(t)) = 12 \sum_{f_1^*} \sum_{f_2^* < f_1^*} Re\left(B_{xxx}(f_1^*, f_2^*)\right) + 6 \sum_{f_1^*} Re\left(B_{xxx}(f_1^*, f_2^*)\right) \qquad (4)$$

Equations 3 and 4 can be normalized by $\left(\overline{u^2}\right)^{3/2}$ to directly relate the bispectrum to skewness. The real part of the bispectra to be presented in this paper are computed with signals which were normalized by $\left(\overline{u^2}\right)^{3/2}$. In this manner, a summation over the real part of the bispectrum recovers the skewness. Figure 2 shows the method of summing over the real part of the bispectrum. The frequency resolution, Δf_1^* and Δf_2^* of the bispectrum plots to be presented are equal. As shown in Figure 2, the bispectrum is divided using lines connecting $(i\,\Delta f_1^*, 0)$ and $(0, i\Delta f_2^*)$ (where $i = 1,2,..,N$). The sum is taken over the region between a pair of lines and is denoted by V_i(where $i = 1,2,..,N$). These values are plotted as shown in Figure 2b. The abscissa is f_{12}^* and its resolution Δf_{12}^* equals Δf_1^*. Thus, the area under the curve will be equal to the skewness.

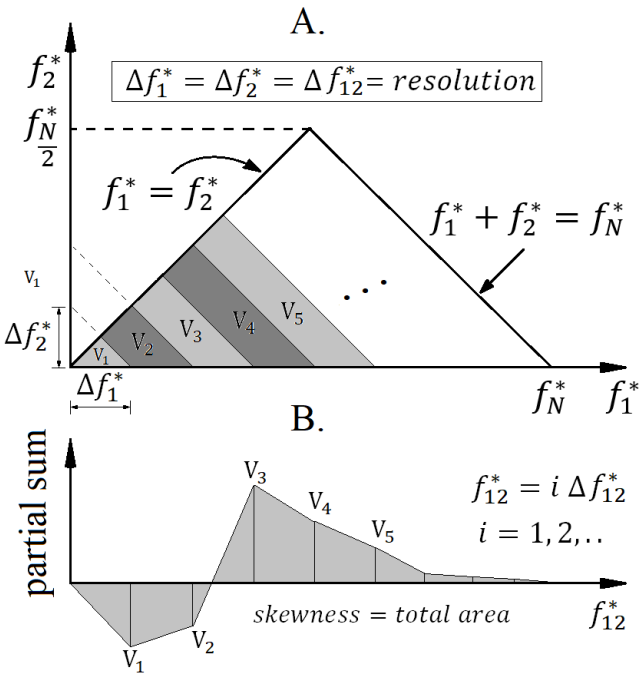

Figure 2. Summation over the real part of the bispectrum to recover skewness.

III. Experimental Facility

The experiments were conducted in a subsonic, open-return wind tunnel in the Hessert Laboratory for Aerospace Rsearch at the University of Notre Dame. The wind tunnel has an inlet with a contraction ratio of 20:1. The inlet has a series of 12 turbulence management screens to condition the flow resulting in freestream turbulence levels of less than 0.1% for frequencies greater than 10 Hz. Air is drawn through the inlet by an eight-bladed fan connected to an 18.6 kW a.c. induction motor. The test section is 0.61 m by 0.61 m in cross section and 1.83 m in length. One test section side wall and a window in the test section ceiling are made from glass to provide optical access to the flow

field. A flat boundary layer development plate 2 meters in length with an elliptic leading edge covered with distributed sand grain roughness was installed in the tunnel. The plate spanned the full width of the test section and was mounted at the tunnel test section mid-height. A constant temperature anemometer (CTA) with a single boundary layer hot-wire probe (Auspex Type-AHWU-100) with 5 μm diameter and sensor length l = 1.5 mm length was used to collect time series streamwise velocity component data. It should be noted that the inner variable normalized length ($l^+ = lu_\tau/\nu$) of the hot-wire sensors were kept below 25 to minimize the effect of spatial averaging and l/d (length to diameter ratio) was maintained around 200. The hot wire sensor was operated in constant temperature mode by a AA lab systems AN-1003 anemometer. A computer controlled traversing stage was inserted through the ceiling of the test section along the midpoint of the tunnel span to allow the hot wire anemometer probe to traverse the test section and make measurements at different wall-normal (y-locations) relative to the boundary layer plate. The hot-wire sensor data was digitized using a National Instruments data acquisition system (NI-USB 6343) having 16 bits analog to digital conversion resolution. For all bispectral computations, a sampling frequency of 30 kHz ($f^*_{sample} = 150$), an FFT blocksize of 8192 and total 1300 blocks were used for the calculations. A series of convergence tests were performed in order to verify that all bispectra were fully converged.

Table 1 summarizes the boundary layer parameters measured x = 1.42 m downstream of the plate leading edge where the bispectral measurements to be presented were taken. The friction velocity u_τ was found using the Clauser method. In all of the experiments described below, the tunnel free stream velocity was $U_\infty = 7$ m/s.

Table 1. Turbulent Boundary Layer Parameters

δ	U_∞	u_τ	C_f	H	Re_θ	Re_τ
35 mm	7.0 m/s	0.298 m/s	0.0037	1.3	1,770	690

Figure 3a presents the boundary layer inner-variable scaled mean velocity profile and Figure 3b the corresponding streamwise component turbulence intensity profile. The mean velocity profile exhibits classic log law of the wall behavior. The center of the logarithmic region is given by $y^+ = \sqrt{15\,Re_\tau} = 102$ (Mathis et al [11]). The turbulence intensity profile shows an inner peak value of $\overline{u^2}/u_\tau^2 \approx 7$ at y^+ =15. Taken together, Table 1 and Figures 3a,b indicate canonical zero pressure gradient turbulent boundary layer development on the plate.

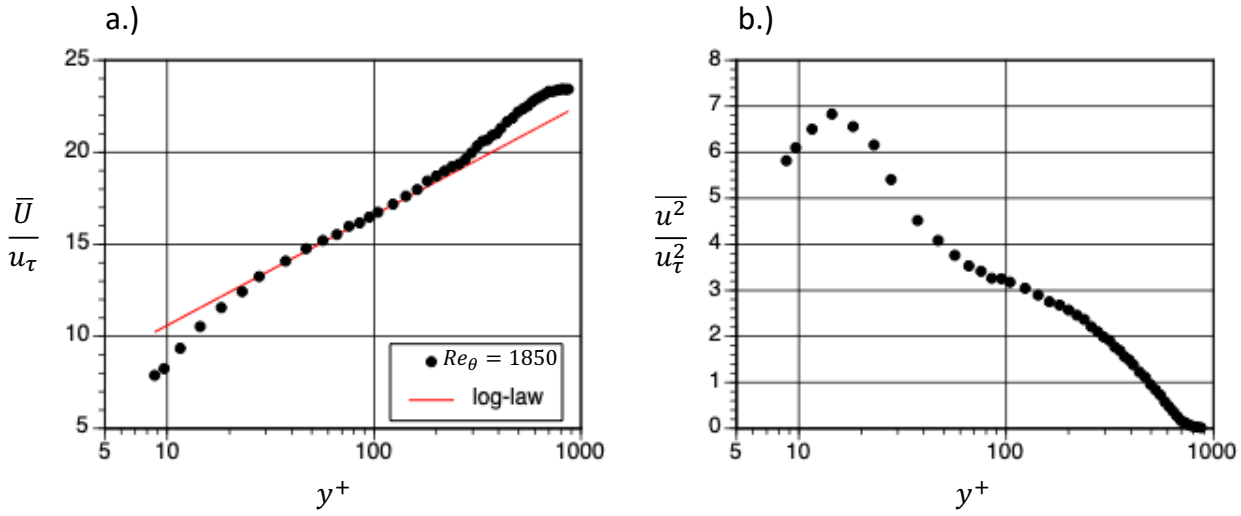

Figure 3. a) inner-variable scaled mean velocity and b) streamwise component turbulence intensity.

Figure 4 presents the skewness profile for the turbulent boundary layer. This figure highlights with the indicated arrows four selected wall-normal locations for which the skewness was spectrally decomposed. The location $y^+ = 8$ is taken as representative of the positive skewness that is typically observed in the near-wall region of turbulent boundary layers. The location $y^+ = 12$ exhibits reduced, but positive skewness. The location $y^+ = 15$ corresponds to the maximum

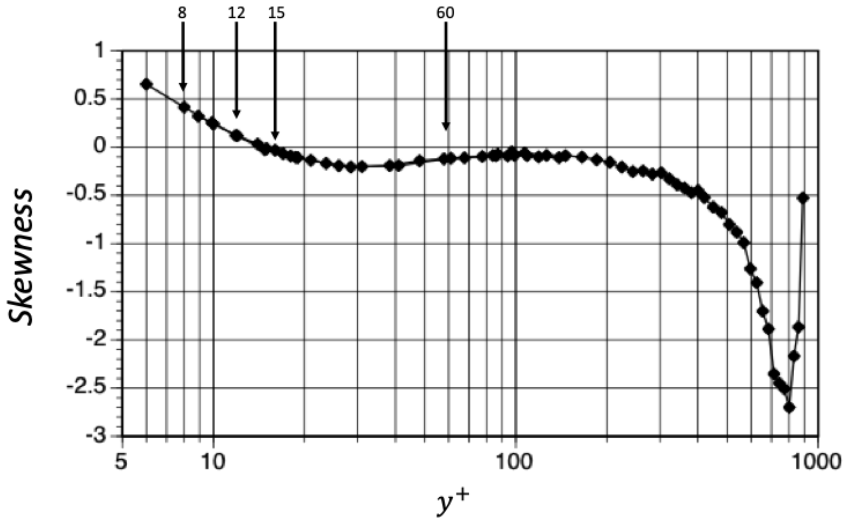

Figure 4. Measured skewness profile for the turbulent boundary layer with wall-normal locations for spectral decomposition of the skewness highlighted.

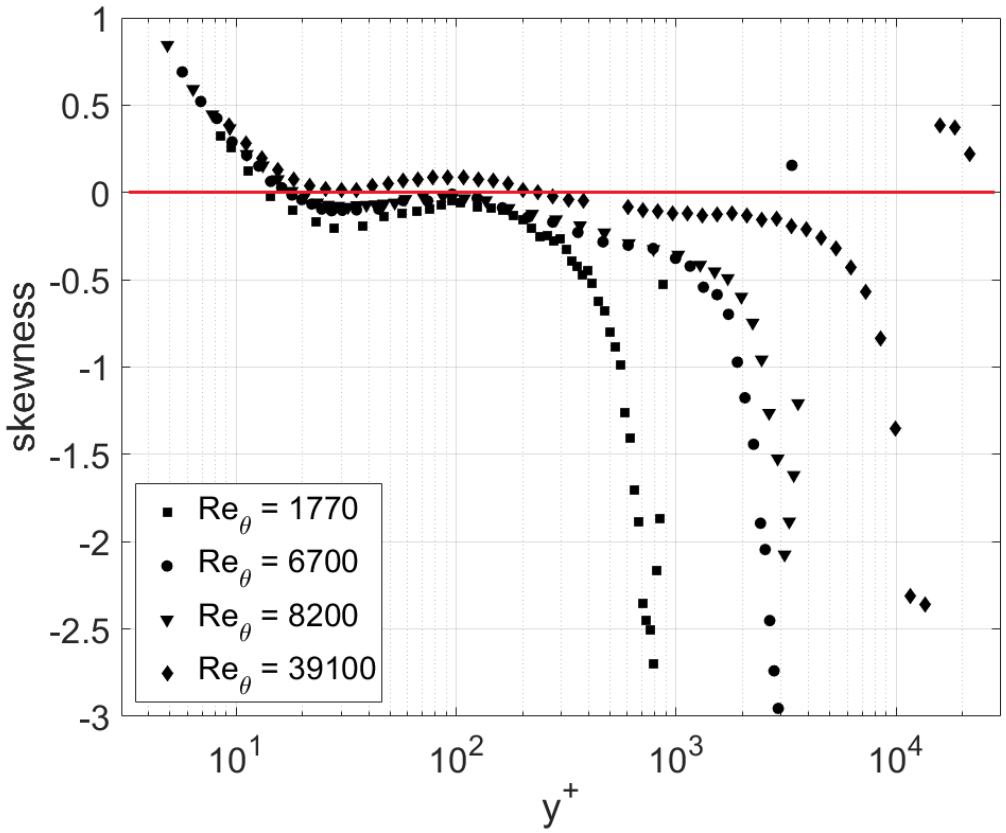

Figure 5. Comparison of zero pressure gradient turbulent boundary layer skewness profiles at four widely varying values of Re_θ.

turbulence intensity location and for which the skewness is very nearly zero. Finally, the location $y^+ = 60$ is representative of the logarithmic region and for which the skewness is negative. That this behavior is not unique to the $Re_\theta = 1{,}770$ turbulent boundary layer investigated here is shown Figure 5 which compares skewness profiles obtained in another wind tunnel facility at the University of Notre Dame at two higher Re_θ values as well as the University of Melbourne wind tunnel facility at $Re_\theta \approx 39{,}100$ (Baars and Marusic [12]).

IV. Experimental Results

A. Conditional Measurements

Previous studies have demonstrated that the near-wall region of the turbulent boundary layer is characterized by discrete, energetic ejection-sweep (hereafter referred to as E-S) and sweep-ejection (hereafter referred to as S-E) events (Runstadler et al 1963, Kline et. al. 1967, Rao et. al. 1971). The variable-interval-time-averaging (VITA) conditional sampling method of Blackwelder and Kaplan (1976) was applied to measured streamwise velocity time series but with the additional distinction in the conditional algorithm between detection of E-S events and the S-E events. The E-S events are found to be an order of magnitude more frequent than S-E events. In both cases an averaging time $\tau^+ = \tau\, u_\tau^2/\nu = 10$ was chosen as the detection window size and a threshold value $\kappa = 1.0$ was selected. These values are fully consistent with those originally employed by Blackewelder and Kaplan (1976). Furthermore, both E-S and the much rarer S-E events can produce signatures that give rise to either positive or negative skewness and these too can be distinguished in the conditional sampling algorithm. As an example, two characteristic burst signatures for E-S events at $y^+ = 8$ are compared in Figure 6. The signature that gives rise to negative skewness is shown as the black curve and is denoted $-V_e$ and that giving rise to positive skewness is shown as the red curve and is denoted $+V_e$. Similar results are found for E-S and S-E events at other near-wall locations.

In addition, there is a change in the degree of asymmetry of both the E-S and S-E event signatures with distance from the wall. This aspect can be seen in Figure 7 which compares E-S VITA signatures at $y^+ = 8$ and $y^+ = 17$. At $y^+ = 8$, the signature is highly asymmetric with the sweep portion of the signal dominant over the ejection. This asymmetry is greatly reduced farther from the wall as is evident from the signature at $y^+ = 17$ which is quite symmetric in amplitude. The near wall skewness is positive (Figure 4) for $y^+ < 15$ and figure 7 shows that the E-S events are asymmetric and dominated by the sweep side. One naturally arising question is how these events contribute to near wall region positive skewness? It will be shown that owing to this asymmetry both events (especially E-S) greatly contribute to the near wall region positive skewness.

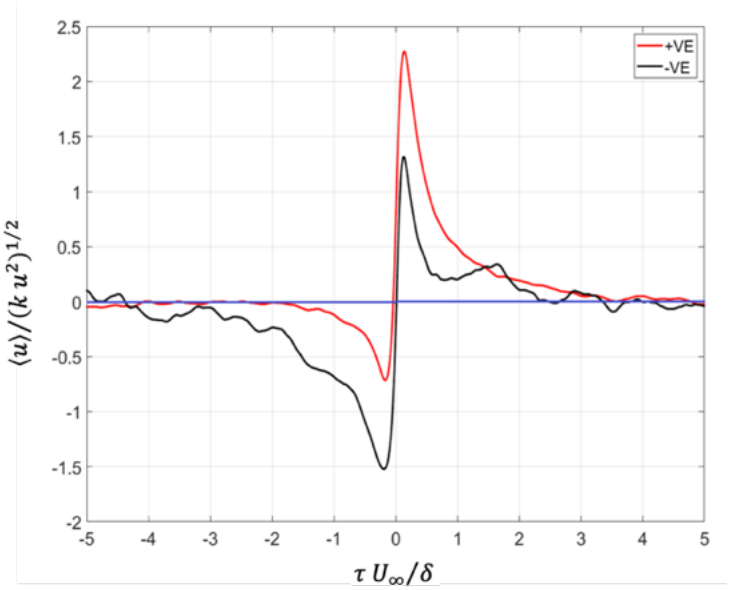

Figure 6. Ejection-sweep event signatures at $y^+ = 8$ giving rise to positive (red curve) and negative skewness (black curve).

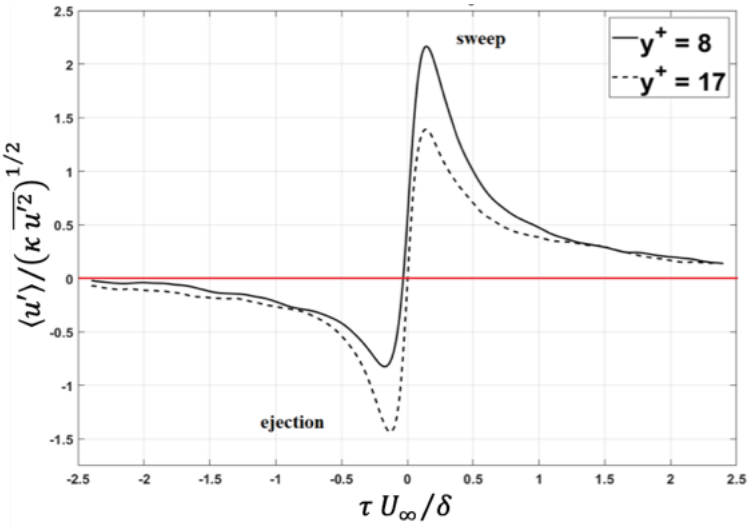

Figure 7. Comparison of ejection-sweep event signatures at y^+ =8 (solid curve) and y^+ = 17 (dashed curve) showing a loss of signature asymmetry with increased distance from the wall.

B. Spectral Decomposition of Skewness Measurements

Figure 8a presents the spectral decomposition of the skewness for the near-wall location $y^+ = 8$. The bispectrum is presented in an f_1^*, f_2^*, subdomain that is a smaller subset of the full region shown in Figure 1 in order to highlight the portion with significant modal content. Also plotted to-scale against the f_1^* abscissa in Figure 8b are the probability density functions (PDF) at $y^+ = 8$ for VITA event frequency, f^*, (including both E-S and S-E events in combination) that result in either positive or negative skewness. The PDF for the frequency of positive skewness events (denoted +Ve) is indicated in red while that associated with negative skewness events (denoted -Ve) is indicated in green and overlays the +Ve with sufficient transparency so that the underlying PDF can still be discerned. It is clear that at y+ = 8 positive skewness E-S and S-E events are much more frequent which is fully consistent with the positive skewness shown in Figure 4 for this location. The mean frequency for +Ve events is is $f_{+ve}^* \approx 0.05$ while that for -Ve events is $f_{-ve}^* = 0.006$.

From Figure 8a it is also apparent that the most significant triad interactions contributing to positive near-wall skewness involve f_1^* and $f_2^* < 0.3$ which is also noted to correspond to the range of most probable frequencies for +Ve burst events. This area is indicated in Figure 8a as the triangular area delineated by the dashed line. Based on the VITA conditional sampling, the mean positive skewness event frequency at $y^+ = 8$ is approximately $f_{+ve}^* \approx 0.05$. It may be noted from Figure 8a that the highest peaks in the real portion of the bispectrum within the dashed region involve triad interactions involving multiples of this frequency: $(i/2)\, f_{+Ve,1}^* + (j/2)\, f_{+Ve,2}^*$, $i = 2,3,4 \ldots$ $j = 2,3,4 \ldots$. Additional contributions to positive skewness is shown associated with $f_1^* = f_2^* < 0.7$ which also corresponds to the frequency range contributing to the probability density function of +Ve burst events. This region of positive skewness is bounded by $f_1^* + f_2^* = 1.4$.

Figure 9 shows the summation over the real part of the bispectrum at $y^+ = 8$ to recover the skewness. This figure shows both the partial (black curve) and cumulative (red curve) bispectral summation as a function of frequency $f_{12}^* \equiv f_1^* + f_2^*$. The partial sum peaks near $f_{12}^* = 0.6$ which is associated with triad interactions within the dashed region shown in Figure 8a and at this frequency the cumulative sum accounts for 36% of the skewness. By $f_{12}^* = 1.4$ the cumulative sum accounts for approximately 77% of the final skewness value.

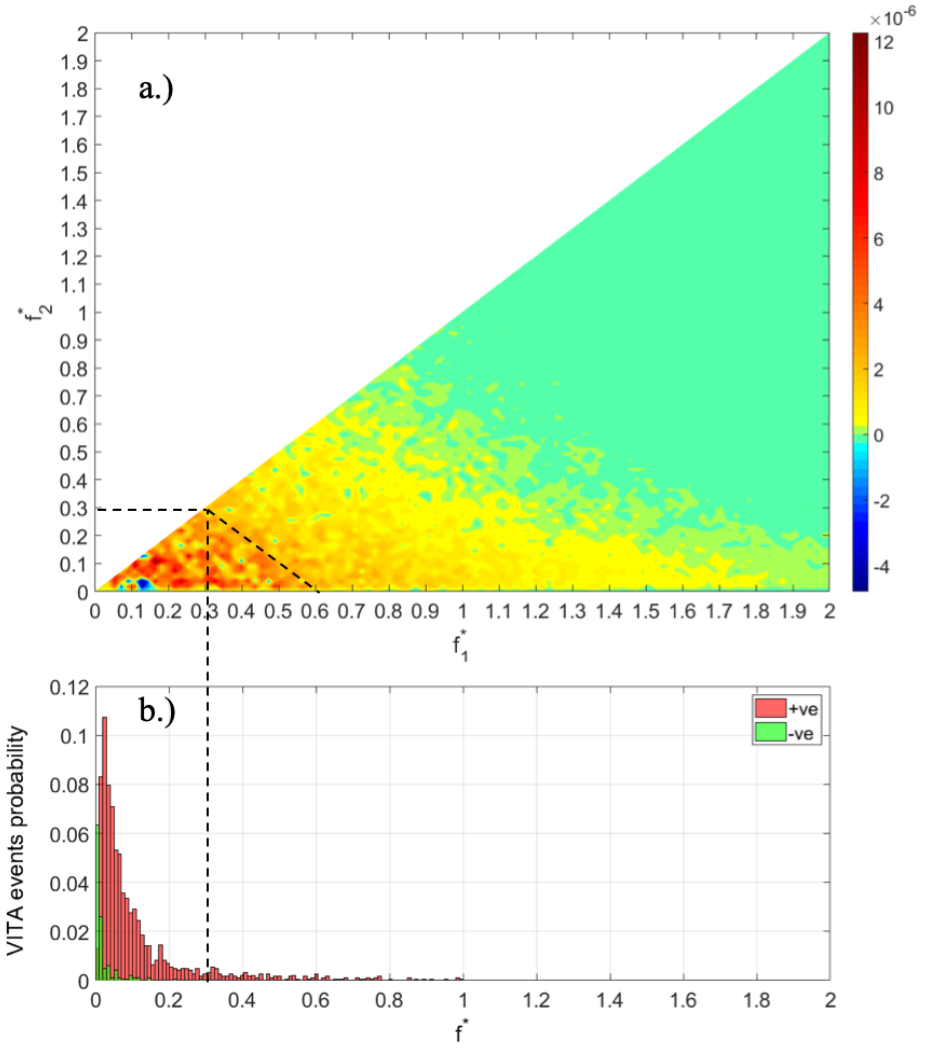

Figure 8. a) Spectral decomposition of skewness at $y^+ = 8$; b) PDFs of the frequency of positive ($+V_e$) and negative ($-V_e$) skewness producing ES and SE events.

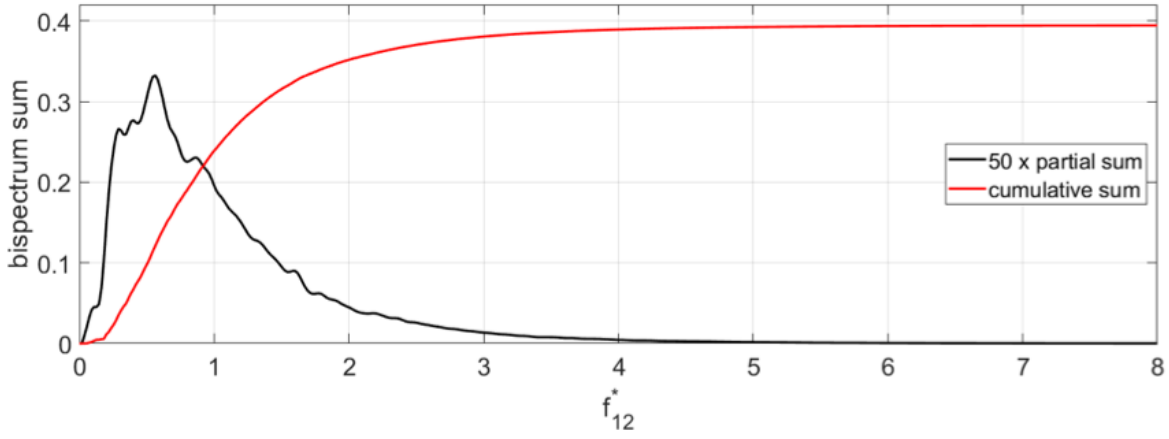

Figure 9. Partial and cumulative summation of the skewness from the real part of the bispectrum at $y^+ = 8$.

Figure 10a presents the spectral decomposition of skewness obtained at y^+ =12. The region of most significant triad interactions remains the same as the frequency range associated with the PDFs for +Ve and -Ve events. At this wall normal location the most probable frequency for +Ve and -Ve events is found to be 0.04 and 0.02, respectively It is notable that several negative peaks are now present in the bispectrum and these are associated primarily with frequencies $f_1^* = f_2^* < 0.2$ which also corresponds to the frequency range contributing most to the probability density function of -Ve events shown in Figure 10b. That is, the region of significant negative skewness is bounded by $f_1^* + f_2^* \approx 0.4$ as indicated by the blue dashed triangular region. Discrete negative peaks appear at $f_{-Ve,1}^* + (j/2)\, f_{-Ve,2}^*$ $j = 2,3,4 \ldots$. The most significant peaks in positive skewness occur in the region $f_1^* + f_2^* < 0.7$ corresponding to the range of frequencies $f_1^*, f_2^* < 0.35$ which the associated PDF shows is the approximate range of most probable frequencies for +Ve events.

Figure 11 presents the partial and cumulative summation over the spectral skewness decomposition at y^+ =12. The peak negative value in the partial sum occurs for $f_{12}^* = 0.16$. This is shown in Figure 10a to be associated primarily with wave triads involving harmonics of the mean -Ve event frequency, $f_{-ve}^* \approx 0.02$. The cumulative sum remains negative until $f_{12}^* = 0.43$. The peak positive value in the partial sum occurs at $f_{12}^* = 0.6$ and is associated primarily with triad interactions involving harmonics of the mean +Ve event frequency. The cumulative sum shows that 35% of the final skewness value is obtained by $f_{12}^* = 1$ and 90% by $f_{12}^* = 3$. Figure 10a shows that the interactions leading to the final values of positive skewness are associated with a range of higher frequencies $f_1^* > 0.7$ interacting primarily with multiples of the mean +Ve event frequency, $f_{+ve}^* \approx 0.04$.

Figure 12a presents the spectral decomposition of skewness at y^+ =15. As before, the dominant interactions are clearly associated with the frequency range shown in the PDFs for +Ve and -Ve events ($f_1^*, f_2^* < 0.3$). Associated Figure 12b presents the E-S and S-E frequency PDFs obtained at $y^+ = 15$ for both +Ve, positive skewness and -Ve, negative skewness producing events. It is clear from this figure that at this wall normal location the relative frequency of both events is now comparable. In fact, the mean frequency for +Ve events is $f_{+ve}^* = 0.031$ and for -Ve events $f_{-ve}^* = 0.029$. This is consistent with the observation from Figure 4 that the skewness is nearly zero at this wall-normal location. In Figure 12a negative peaks are present in this region for $f_1^* < 0.3$ and $f_2^* < 0.15$. Examination of the ordinate scale shows that the negative peaks clearly dominate the positive peaks in this region.

Figure 13 shows the partial and cumulative sum over the real part of the bispectrum at $y^+ = 15$. As a consequence of the negative peaks shown in Figure 12a the partial sum reaches a peak negative value at $f_{12}^* = 0.16$ and this is followed by a rapid rise which is largely complete by $f_{12}^* \approx 0.6$. The skewness partial sum takes on positive values for $f_{12}^* > 1.25$. This figure reinforces the idea that the negative contributions to skewness are confined to low frequencies commensurate with the frequency range of -Ve events while positive contributions to skewness involve interactions between modes near the mean +Ve frequency a broad range of higher frequency modes.

The spectral decomposition of skewness at $y^+ = 60$ is shown in Figure 14a and demonstrates a clear dominance of triad interactions producing negative skewness at this wall normal location. The event PDFs obtained at $y^+ = 60$ for both +Ve, positive and -Ve, negative skewness producing E-S and S-E events are presented in Figure 14b. This figure shows the significantly increased frequency of negative skewness producing events relative to those producing positive skewness. The mean frequency for +Ve events is $f_{+ve}^* = 0.049$ and for -Ve events $f_{-ve}^* = 0.076$ at this wall normal location. Consistent with this, the dominant interactions involve multiples of the mean frequencies for both +Ve and -Ve events with interactions producing negative skewness clearly dominating.This is also apparent from examination of the partial and cumulative summation of the bispectrum presented in Figure 15. This figure shows evidence of both positive and negative interactions with the overall dominance of triad interactions producing negative skewness. By $f_{12}^* = 2.0$ the cumulative sum has reached 90% of its final value.

V. Conclusion

Measurement of the spectral decomposition of skewness via the real part of the bispectrum indicates that the frequency range over which triadic interactions occur at each wall normal location investigated is intimately related to the range of frequencies in the associated PDFs for the frequency of +Ve and -Ve E-S and the rarer S-E events. In fact, the dominant triadic interactions in each case are shown to be closely associated with integer and half-integer multiples of the +Ve and -Ve mean event frequencies. In the near wall region (e.g. $y^+ = 8$) the spectral decomposition of skewness is dominated by multiple triadic interactions producing positive skewness. Consistent with this, is the observation that at this location, E-S and S-E event signatures show a distinct asymmetry in which the high-speed sweep portion of the event signature is dominant over the ejection portion which would give rise to local positive

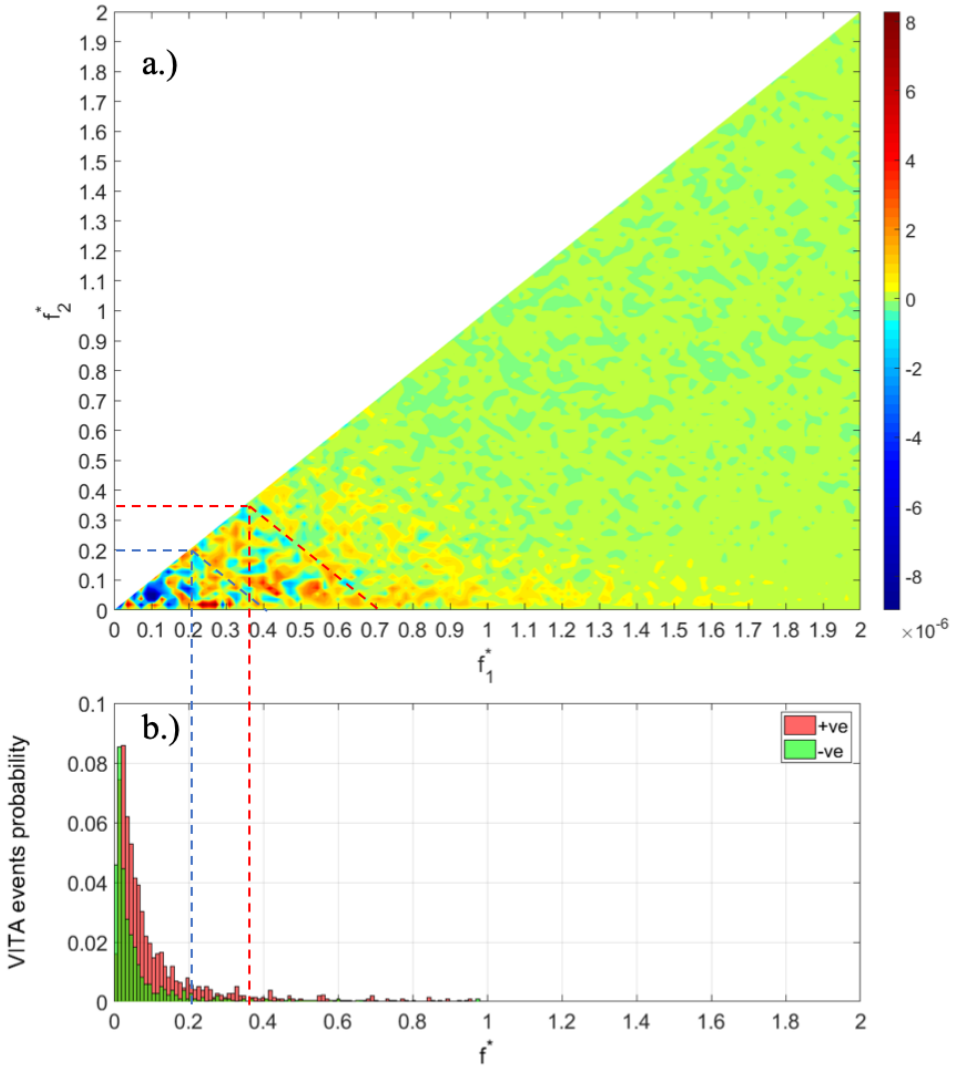

Figure 10. a) Spectral decomposition of skewness at $y^+ = 12$; b) PDFs of the frequency of positive ($+V_e$) and negative ($-V_e$) skewness producing ES and SE events.

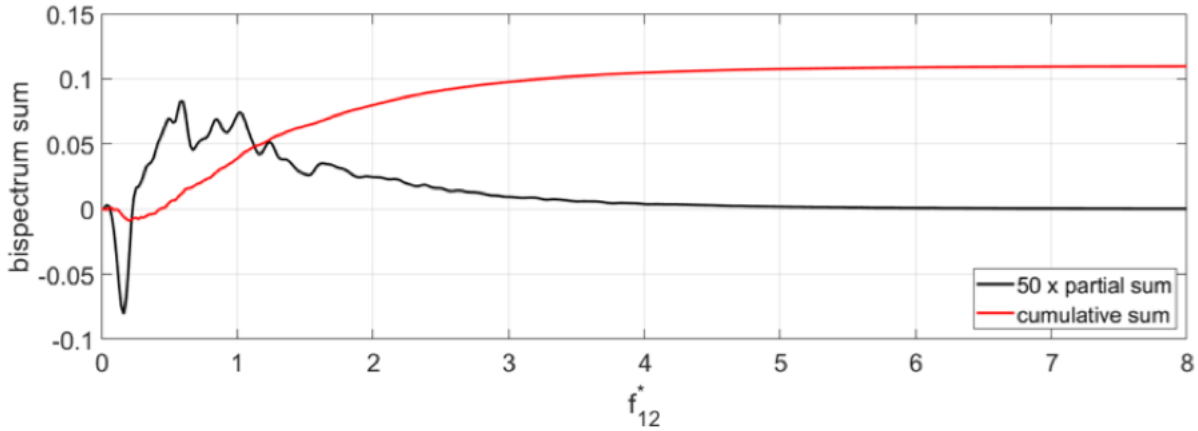

Figure 11. Partial and cumulative summation of the real part of the bispectrum for $y^+ = 12$.

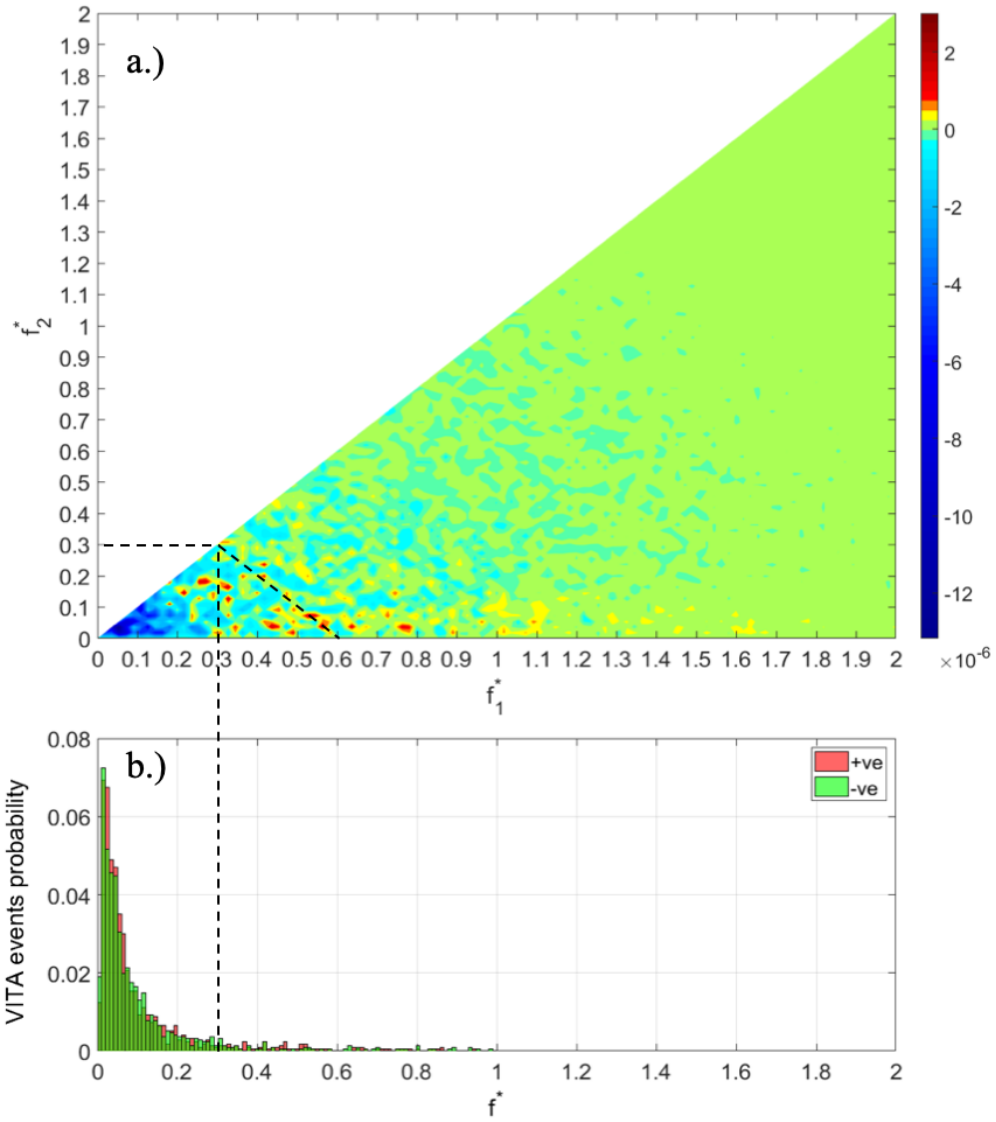

Figure 12. a) Spectral decomposition of skewness at y^+ = 15; b) PDFs of the frequency of positive ($+V_e$) and negative ($-V_e$) skewness producing ES and SE events.

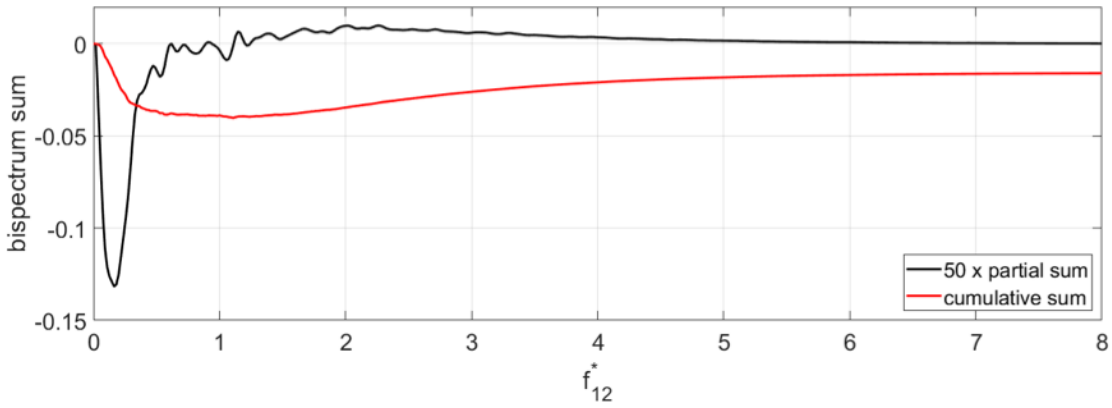

Figure 13.. Partial and cumulative summation of the real part of the bispectrum for y^+ = 15.

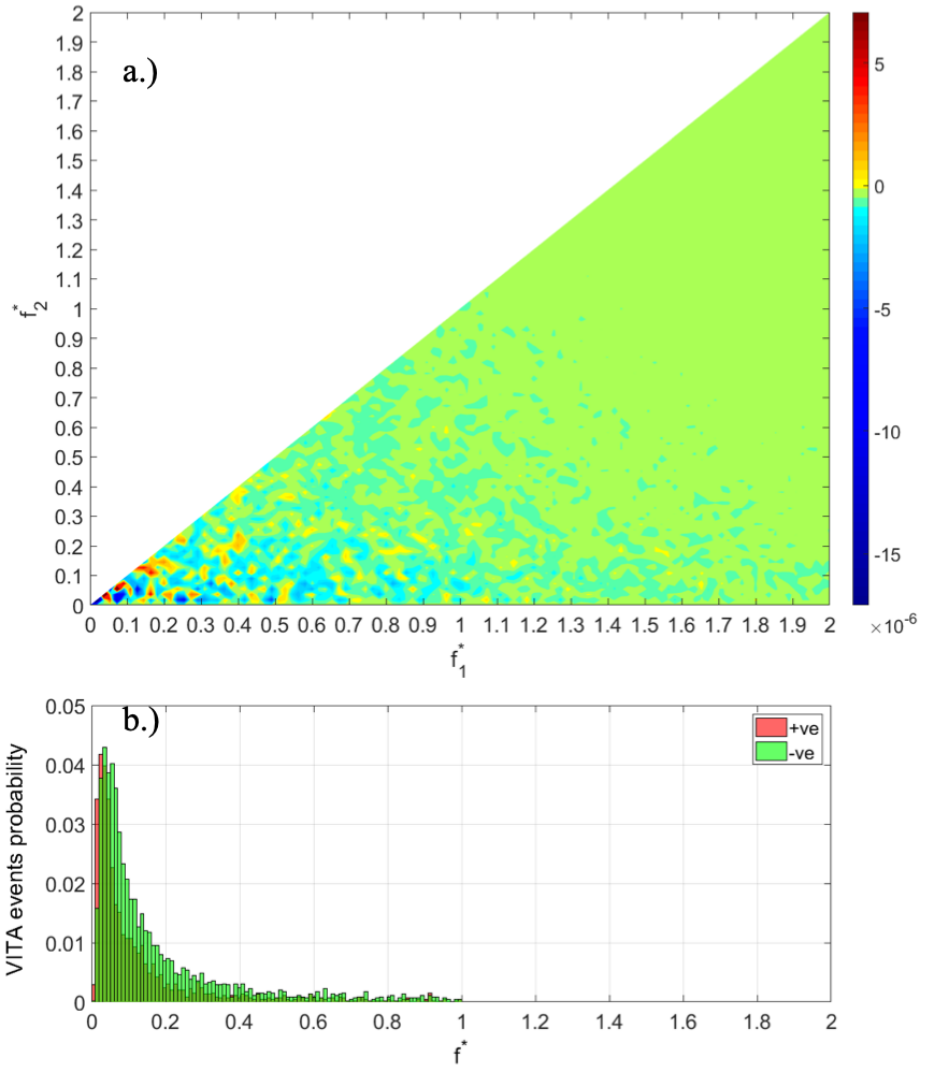

Figure 14. a) Spectral decomposition of skewness at y^+ = 60; b) PDFs of the frequency of positive ($+V_e$) and negative ($-V_e$) skewness producing ES and SE events.

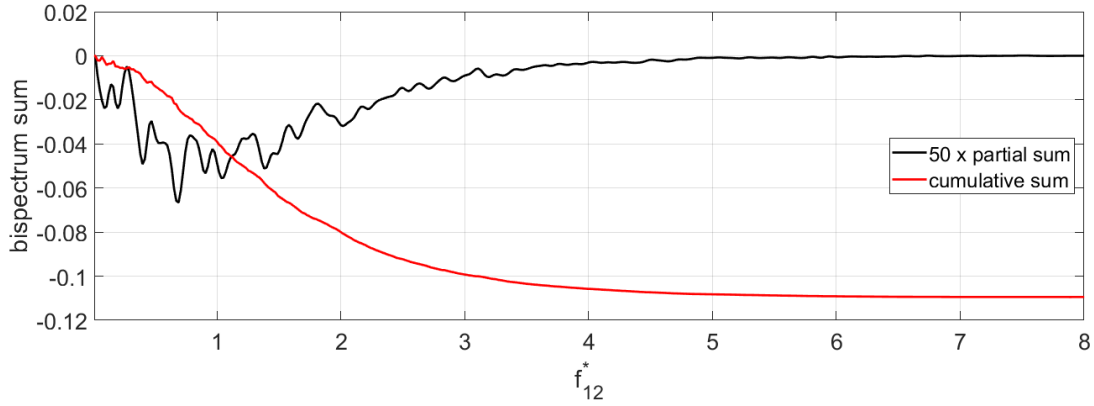

Figure 15. Partial and cumulative summation of the real part of the bispectrum for y^+ = 60.

skewness. Such wall-directed fluid motion and associated so-called "splatting events" is a known source of high viscous drag in the turbulent boundary layer as discussed by Kim [17] and Duong el al [18]. Somewhat farther from the wall (e.g. y^+ =12) the spectral decomposition of skewness shows a mix of both positive and negative skewness producing triad interactions consistent with increased -Ve event frequency in the associated PDFs. This pattern continues with increased distance from the wall and at y^+ =15 the spectral decomposition of skewness shows a nearly equal mix of both positive and negative skewness producing triad interactions and this is commensurate with nearly equal mean frequencies for both +Ve and -Ve events in the associated event PDFs. It is also worthy of note that at these locations the partial summation over the real part of the bispectrum (e.g. Figures 19 and 22) shows that the negative contribution to skewness always occurs over a range of lower frequencies than the positive components which is physically consistent with the concept that the source of the negative skewness is due to an upwelling of low velocity fluid from the region nearer the wall. Conversely, the positive interactions involve multiples of the mean +Ve event frequency with significantly higher frequency modes and the resulting positive contribution to skewness generally dominates the higher frequency range in the skewness partial sum. This also suggests the importance of discrete sweep events associated with transport of higher velocity fluid toward the near-wall region.

With increased distance from the wall the pattern of the increased importance of negative interactions continues and in the log layer at y^+=60 the partial sum is shown to be dominated by negative skewness values. The associated event frequency PDFs show that the mean frequency of -Ve events now exceeds that of +Ve events. The dominant triad interactions contributing to negative skewness involve multiples of the -Ve mean event frequency with a wide range of higher frequencies and this is reflected in the skewness partial sum shown in Figure 15.

Inspection of the bispectral plots indicates that the scaled frequencies associated with the locally dominant triad interactions are bounded within $f^* \leq O(0.4)$ and this generally matches the frequency band associated with the VITA event PDFs. When these frequencies are converted to a streamwise wavelength using the local mean velocity as the convective speed, the associated wavelengths are $\lambda_x^+ \sim O(1000)$. This suggests that the dominant triad interactions are a manifestation of the influence of the overlying buffer layer streamwise vortical structures. This is also fully consistent with the observed dominance of positive skewness interactions near the wall and the more gradual importance of negative skewness interactions with increasing y^+. The cumulative and partial skewness summations show that most of the final skewness value is recovered by $f^* \sim O(2)$ which corresponds to a streamwise wavelength $\lambda_x^+ \sim O(200)$.

Future work will involve the use of a plasma-based, Active Large-Scale Structure Actuator (ALSSA) device to modify the outer dynamics of the boundary layer as reported by Lozier et al (2020). The device utilizes an ac-dielectric barrier discharge plasma actuator operated in a periodic manner in order to introduce organized large-scale vortical structures into the outer portion of the boundary layer. Spectral decomposition of the skewness in the actuated turbulent boundary layer will allow the direct influence of outer layer structures to be assessed.

Acknowledgments

This work was supported by Office of Naval Research, Grant number N00014-18-1-2534. This support is gratefully acknowledged.

References

[1] S. K. Robinson, "Coherent Motions in the Turbulent Boundary Layer," *Ann. Rev. Fluid Mech.,* vol. 23, pp. 601-639, 1991.

[2] N Hutchins and I Marusic. Evidence of very long meandering features in the logarithmic region of turbulent boundary layers. *J. Fluid Mech.*, 579:1–28, 2007a.

[3] N. Hutchins and I. Marusic. Large-scale influences in near-wall turbulence. *Philos. Trans. R. Soc. A*, 365(1852):647–664, 2007b.

[4] Mathis, R., Hutchins, N., and Marusic, I., Lrge-scale amplitude modulation of the small-scale structures in turbulent boundary layers, J. Fluid Mech., Vol. 681, p. 311,2009.

[5] Mathis, R., Marusic, I., Hutchins, N. and Sreenivasan, K. R., The relationship between the velocity skewness and the amplitude modulation of the small scale by the large scale in turbulent boundary layers, Physics of Fluids, 23, 121702, 2011.

6] Rosenblatt, M.; Ness, J. W. Van., Estimation of the Bispectrum, Ann. Math. Statist. 36 (1965), no. 4, 1120--1136. doi:10.1214/aoms/1177699987.

[7] Kim, Y. C. and Powers, E. J., "Digital Bispectral Analysis and Its Applications to Nonlinear Wave Interactions," in *IEEE Transactions on Plasma Science,* vol. 7, no. 2, pp. 120-131, June 1979, doi: 10.1109/TPS.1979.4317207.

[8] Elgar, S., Relationships Invovling Third Moment and Bispectra of a Harmonic Process, IEEE Transactions on Acoustics and Signal Processing, Vol. ASSP-35, No. 12, pp 1725-1726, 1987.
[9] Rosenblatt, M.; Ness, J. W. Van. Estimation of the Bispectrum. Ann. Math. Statist. 36, no. 4, 1120--1136. doi:10.1214/aoms/1177699987, 1965.
[10] Elgar, S., Relationships Invovling Third Moment and Bispectra of a Harmonic Process, IEEE Transactions on Acoustics and Signal Processing, Vol. ASSP-35, No. 12, pp 1725-1726, 1987.
[11] R. Mathis, N. Hutchins, and I. Marusic, "A predictive inner–outer model for streamwise turbulence statistics in wall-bounded flows," J. Fluid Mech., 681, pp. 537–566, 2011.
[12] Baars, W. J., Marusic, I. Data-driven decomposition of the streamwise turbulence kinetic energy in boundary layers. Part 1. Energy spectra, J. Fluid Mech., Vol. 882, A25, 2020.
[13] Runstadler, P. W., Kline, S. J. & Reynolds, W. C. 1963 Mech. Engrg Dept. Rept. MD-8, Stanford University.
[14] Kline, S. J., Reynolds, W. C., Schraub, F. A. AND Runstadler, S. P. W.,The structure of turbulent boundary layers. J. Fluid Mech. vol. 30, part 4, pp. 741-773, 1967.
[15] Rao, K. N., Narasimha, R. & Badrinaraynan, M. A. , The bursting phenomenon in a turbulent boundary layer. J. Fluid Mech. 48, 339, 1971.
[16] Blackwelder, R.F., Kaplan, R.E. On the wall structure of the turbulent boundary layer, J. Fluid Mech., Vol. 76, pp. 89-112, 1967.
[17] Kim, J., Physics and control of wall turbulence for drag reduction, Philo. Tran. of the Royal Society A: Mathematical, Physical and Engineering Sciences, 369, 1940, 1396-1411, 2011.
[18] Duong, A., Corke, T., & Thomas, F., (2021). Characteristics of drag-reduced turbulent boundary layers with pulsed-direct-current plasma actuation, *Journal of Fluid Mechanics*, 915, A113. doi:10.1017/jfm.2021.167